Astronomy & Astrophysics manuscript no. output
April 28, 2024

Challenging the single star evolution scenario of Be-stars with MESA

N. Van Wouwe[1], A. Picco[1], and O. Verhamme[1]

Institute of Astronomy, KU Leuven, Celestijnlaan 200D, 3001 Leuven, Belgium
e-mail: nick.vanwouwe@student.kuleuven.be

This is a project for the course 'theoretical research projects' from the Master Astronomy & Astrophysics at KU Leuven.

ABSTRACT

Context. Be stars are rapidly rotating B main sequence stars that show line emission due to a decretion disk. An important factor in the rotational, and overall, evolution of a star is the mass loss it experiences due to radiation-driven winds.
Aims. We aim to investigate the possibility of single-star evolution channels in the formation of Be stars by comparing two different wind prescriptions, where one is characterised by stronger winds and a bi-stability jump (Vink wind), while the other one predicts weaker winds and no bi-stability jump (Björklund wind).
Methods. Using the MESA code, we evolve a grid of stars through their whole main sequence stage, for both wind prescriptions and LMC and Milky Way metallicity. This grid is varied in initial mass $5M_\odot \leq M_{\rm ZAMS} \leq 30M_\odot$ and initial rotational velocity at the equator $0.1 \leq v_{\rm rot}/v_{\rm crit} \leq 0.8$. These models are then analysed in function of their mass loss trough stellar winds and its impact on the rotational evolution of the star.
Results. Our simulations demonstrate that the Björklund wind prescription significantly enhances the potential for stars to reach higher rotational velocities conducive to Be star formation, due to its characteristically lower mass loss rates.

Key words. stars: massive – stars: winds – stars: evolution – stars: Be stars

1. Introduction

Be stars, classified within the B-type main sequence, are characterised by a spectrum that shows strong hydrogen emission lines and infrared excess. These features indicate the presence of a circumstellar decretion disk, hypothesised to form as material is expelled from the star facilitated by its rapid rotation. The idea that Be stars are rapid rotators was initially proposed by Struve (1931) and continues to be supported by more recent studies, such as by Rivinius et al. (2013). However, the precise rotational velocity required for a B-type star to create and maintain a decretion disk is unclear.

As discussed in Hastings et al. (2020), it is expected that the equatorial rotation velocity $v_{\rm rot}$ needs to be a significant fraction of the critical rotation velocity $v_{\rm crit}$, which is defined as the rotational velocity at which material at the equator becomes unbound. Based on observations, Huang et al. (2010) suggests that this process is mass-dependent. Their results indicate that low-mass B-type stars ($< 4M_\odot$) require a high rotational velocity $v_{\rm rot}/v_{\rm crit} > 0.96$ to become Be stars, while it drops to $v_{\rm rot}/v_{\rm crit} > 0.64$ for higher mass stars ($> 8.6M_\odot$). Zorec et al. (2016) found that Be phenomena are characterised by a wide range of true velocity ratios $0.3 \lesssim v_{\rm rot}/v_{\rm crit} \lesssim 0.95$ with the mode of distribution being 0.65, which suggests that the probability that Be stars are critical rotators is extremely low. On the contrary, Townsend et al. (2004) argues that Be stars could be rotating near or at critical velocities as previous studies have not fully taken into account the effects of gravity darkening.

The mechanisms that lead to high rotational velocities in stars can be categorised into those arising from single and binary star models. In binary systems, interactions with a mass transfer phase can significantly increase a star's rotational speed, a phenomenon supported by the observation of over 100 Be/X-ray binary systems (Raguzova & Popov 2005). For single stars, the models must account for the interaction between the contracting core, which spins up due to the conservation of angular momentum, and the expanding envelope. This interaction necessitates the transfer of angular momentum from the core to the envelope. The transfer can be facilitated by viscous forces acting between different layers of the star or by internal magnetic fields. A notable example of an efficient angular momentum transport mechanism within stars is the Tayler-Spruit dynamo (Spruit 2002).

While the transport of angular momentum from the core to the envelope causes the star's surface to spin up, any further transport of angular momentum outside the star will slow it down. As stellar winds strip material from the surface, this material, moving along external magnetic fields, will decelerate the star. This underlines the importance of the wind prescription used in single-star evolution models regarding the formation of Be stars. In the paper "The single star path to Be stars" (Hastings et al. 2020), population synthesis was conducted using evolutionary models of rotating massive main-sequence stars (Brott et al. 2011), which utilised a wind prescription primarily based on the mass loss predictions by Vink et al. (2001). In our study, we will compare the Vink wind prescription implemented in MESA, designed to recreate the results from Brott et al. (2011), to a newer wind prescription proposed by Björklund et al. (2022).

Section 2 introduces the wind prescriptions and their implementation within the MESA code. Section 3 outlines the methodology employed in this project. The results of the simulations are discussed in Section 4, and conclusions are drawn in Section 5.

2. Wind prescriptions

2.1. Vink wind

We will refer to the wind prescription implemented in MESA, which replicates the evolutionary tracks from Brott et al. (2011), as the 'Vink wind'. This prescription is primarily based on the mass loss predictions of Vink et al. (2001) and is supplemented by two additional mass loss models to address specific scenarios. The first supplementary model, derived from Nieuwenhuijzen & de Jager (1990), addresses an increase in mass loss as stars approach the Humphreys-Davidson limit. The second, based on the work of Hamann et al. (1995), considers the effects of surface enrichment. For a comprehensive explanation and justification of this combination of wind prescriptions, we direct readers to section 2.2, Mass loss, in Brott et al. (2011).

The mass loss determined in Vink et al. (2001) is characterised by a bi-stability jump at a certain temperature, which corresponds to the recombination of Fe IV to Fe III, with the latter being a more efficient line driver, significantly enhancing the mass loss. This temperature is implemented in MESA by the following formula:

$$T_{\rm eff}^{\rm jump} = 10^3 \left[61.2 + 2.59\left(-13.636 + 0.889 \log_{10}(Z_*)\right)\right]$$

Which depends on the metallicity Z_*, which is expressed in solar metallicity $Z_\odot$. In MESA, we calculate this value based on a normalized metal content, which can be determined by the iron mass fraction at the surface $S_{\rm Fe}$, divided by a constant:

$$Z_*^{\rm MESA} = S_{\rm Fe}/(1.0116465653352326 \times 10^{-3})$$

Using this value we can calculate the jump temperatures for both metallicities:

- LMC: $S_{\rm Fe} \approx 7.75 \times 10^{-4} \;\rightarrow\; T_{\rm eff}^{\rm jump} \approx 25\,616$ K
- GAL: $S_{\rm Fe} \approx 1.47 \times 10^{-3} \;\rightarrow\; T_{\rm eff}^{\rm jump} \approx 26\,259$ K

The choice between wind models is based on the effective temperature $T_{\rm eff}$. The mass loss values for the individual wind models are denoted by `Vink`, `Nieuwenhuijzen`, and `Hamann`.

Low-Temperature Wind: for $T_{\rm eff} < 0.95\ T_{\rm eff}^{\rm jump}$, the maximum of the `Nieuwenhuijzen` and `Vink` winds is used.

$$\text{wind}_{\rm lowT} = \max(\texttt{Nieuwenhuijzen}, \texttt{Vink}) \tag{1}$$

High-Temperature Wind: for $T_{\rm eff} \geq 1.05\ T_{\rm eff}^{\rm jump}$, a blend of `Vink` and `Hamann` winds is used.

$$\text{wind}_{\rm highT} = \alpha\ \texttt{Vink} + (1-\alpha)\ \texttt{Hamann}/10 \tag{2}$$

Where α is determined by the hydrogen fraction at the surface X_s.

- $X_s > 0.7 \;\rightarrow\; \alpha = 1$
- $X_s < 0.4 \;\rightarrow\; \alpha = 0$
- $0.4 < X_s < 0.7 \;\rightarrow\; \alpha = (X_s - 0.4)/0.3$

Transitional Window: within a 10% window around $T_{\rm eff}^{\rm jump}$, the wind model transitions from low-temperature to high-temperature prescriptions.

$$\text{wind}_{\rm transition} = \beta\ \text{wind}_{\rm lowT} + (1-\beta)\ \text{wind}_{\rm highT} \tag{3}$$

Where β is determined by $T_{\rm eff}$:

$$\beta = \frac{T_{\rm eff}^{\rm jump} + 0.05\ T_{\rm eff}^{\rm jump} - T_{\rm eff}}{0.1\ T_{\rm eff}^{\rm jump}}$$

The mass loss values of the individual wind models are based on several stellar values, where only the `Vink` mass loss has two different formulas depending on the temperature.

The mass loss values:

$$\texttt{Vink} = \gamma\ \dot{M}_{\texttt{hotVink}} + (1-\gamma)\ \dot{M}_{\texttt{coolVink}}$$

$$\texttt{Nieuwenhuijzen} = \dot{M}_{\texttt{Nieuwenhuijzen}}$$

$$\texttt{Hamann} = \dot{M}_{\texttt{Hamann}}$$

With:

$$\begin{aligned}\log_{10}\left(\dot{M}_{\texttt{hotVink}}\right) = &-6.697 + 2.194 \log_{10}\left(L_*/10^5\right) \\ &- 1.313 \log_{10}\left(M_*/30\right) \\ &- 1.226 \log_{10}\left(2.6 \times Z_*^{0.13}\right) \\ &+ 0.933 \log_{10}\left(T_{\rm eff}/40\,000\right) \\ &- 10.92 \left(\log_{10}\left(T_{\rm eff}/40\,000\ {\rm K}\right)\right)^2 \\ &+ 0.85 \log_{10}(Z_*)\end{aligned}$$

$$\begin{aligned}\log_{10}\left(\dot{M}_{\texttt{coolVink}}\right) = &-6.688 + 2.210 \log_{10}\left(L_*/10^5\right) \\ &- 1.339 \log_{10}\left(M_*/30\right) \\ &- 1.601 \log_{10}\left(2.6 \times Z_*^{0.13}\right) \\ &+ 1.07 \log_{10}\left(T_{\rm eff}/20\,000\ {\rm K}\right) \\ &+ 0.85 \log_{10}(Z_*)\end{aligned}$$

and γ is based on $T_{\rm eff}$

- $T_{\rm eff} > 27\,500 \;\rightarrow\; \gamma = 1$
- $T_{\rm eff} < 22\,500 \;\rightarrow\; \gamma = 0$
- $22\,500 < T_{\rm eff} < 27\,500$:
  - $T_{\rm eff} > T_{\rm eff}^{\rm jump} + 100 \;\rightarrow\; \gamma = 1$
  - $T_{\rm eff} < T_{\rm eff}^{\rm jump} - 100 \;\rightarrow\; \gamma = 0$
  - $T_{\rm eff}^{\rm jump} - 100 < T_{\rm eff} < T_{\rm eff}^{\rm jump} + 100 \;\rightarrow\; \gamma = \frac{T_{\rm eff} - T_{\rm eff}^{\rm jump} - 100}{200}$

$$\begin{aligned}\log_{10}\left(\dot{M}_{\texttt{Nieuwenhuijzen}}\right) = &-14.02 + 1.24 \log_{10}(L_*) \\ &+ 0.16 \log_{10}(M_*) \\ &+ 0.81 \log_{10}(R_*)\end{aligned}$$

$$\begin{aligned}\log_{10}\left(\dot{M}_{\texttt{Hamann}}\right) = &-11.95 + 1.5 \log_{10}(L_*) \\ &- 2.85\ X_s \\ &+ 0.85 \log_{10}(Z_*)\end{aligned}$$

Where the parameters L_*, M_*, and R_* are in solar units and Z_* is taken as $Z_*^{\rm MESA}$.

2.2. Björklund wind

We will refer to the theoretical mass loss rates as determined in Björklund et al. (2022) as the 'Björklund wind'. This prescription not only finds much lower mass loss rates compared to Vink et al. (2001), it also shows no sign of a bi-stability jump. The two only start to converge for very high temperatures ~ 60 000 K.

$$\begin{aligned}\log_{10}\left(\dot{M}_{\texttt{Björklund}}\right) = & \\ & -5.52 \\ & +2.39\log_{10}\left(L_*/10^6\right) \\ & -1.48\log_{10}\left(M_*/45\right) \\ & +2.12\log_{10}\left(T_{\rm eff}/45\,000\,{\rm K}\right) \\ & +\left[0.75-1.87\log_{10}\left(T_{\rm eff}/45\,000\,{\rm K}\right)\right]\log_{10}\left(Z_*\right)\end{aligned} \tag{4}$$

Because the Björklund mass loss prescription is aimed at higher temperatures, it is only switched on from 12 000 K. Under that temperature the mass loss is given by The Reimers prescription (Baschek et al. 1975).

$$\dot{M}_{\texttt{Reimers}} = 10^{-13}\ L_*\,R_*\,M_*^{-1}$$

3. Methodology

To investigate the impacts of different wind prescriptions in the context of forming Be stars, we simulated the main-sequence evolution of a grid of stellar models. The models were varied along four parameters:

- Wind prescription: Vink and Björklund wind.
- Metallicity: LMC and Milky Way (GAL).
- Initial equatorial rotation in terms of the critical rotation: $v_{\rm rot}/v_{\rm crit} \in [0.1,\ 0.2,\ ...,\ 0.8]$
- Initial mass: $M/M_\odot \in [5,\ 6,\ ...,\ 30]$

The simulations were conducted using the 1D stellar evolution code, Modules for Experiments in Stellar Astrophysics (MESA), version *r24.02.1-rc1* (Paxton et al. 2010, 2013, 2015, 2018, 2019). An adjustment was made to the MESA code to mitigate mass loss during the relaxation phase, which was significant when using the Björklund wind. This adjustment ensured that all simulations started at their predefined initial masses when entering the Zero Age Main Sequence (ZAMS) phase.

The 832 simulations spanning our entire grid were then analysed in function of their mass loss and rotational evolution. As we wanted to compare our results to Hastings et al. (2020), we chose to apply the Björklund wind to masses reaching lower than the defined ranges in Björklund et al. (2022). We go to $5M_\odot$ as opposed to the lower limit of $15M_\odot$.

4. Results

Inspired by Fig. 2 from Hastings et al. (2020), most figures will contain the masses 5, 15, and $25M_\odot$, representing the lower, middle, and higher masses considered in our grid.

4.1. HR tracks

In Fig. 1 the Herzsprung-Russel (HR) tracks are plotted for masses in steps of $5M_\odot$. Each panel represents a different initial equatorial velocity in terms of the critical velocity:

$v_{\rm init} = v_{\rm rot}/v_{\rm crit}$ at ZAMS

We will further refer to this value simply as 'initial rotation'.

The orange dashed line represents the activation temperature of the Björklund wind, which is set to 12 000 K, as stated before. Only a couple of tracks cross this boundary. This means that all simulations with the Björklund wind evolve through the main sequence with the Björklund mass loss prescription (Eq. 4), except for a couple of lower mass stars at high initial rotation at the end of their main sequence evolution ($t/t_{MS} \sim 0.99$).

The green bands represent the window where the Vink wind transitions (Eq. 3) from its high-temperature wind (Eq. 2) to its low-temperature wind (Eq. 1). The light green shows the window for GAL metallicity and dark green the LMC metallicity. For higher initial rotations $v_{\rm init} \geq 0.5$, we can clearly notice this jump by a bump in the HR tracks, corresponding to a more abrupt increase in mass loss through stellar winds.

Most evolutionary tracks follow the anticipated trajectories. However, exceptions are observed in the 29 and $30M_\odot$ tracks under the Björklund wind prescription at LMC metallicity with an initial rotation of 0.8 (lower right panel of Fig. 1, only $30M_\odot$ plotted). These tracks exhibit a distinct leftward and upward evolution in the HR diagram. This behavior is attributed to the strong rotational mixing induced by the high rotational speeds of these stars, which promotes chemically homogeneous evolution. As a result, these stars do not develop a contracting core and an expanding envelope. Consequently, they do not undergo the typical cooling and expanding phase but instead increase in luminosity over time. This behaviour, combined with strong stellar winds that expose the hotter inner layers, accounts for their unique trajectories on the HR diagram.

4.2. Mass loss evolution

In Fig. 2 the mass loss rates are plotted for 5, 15, and $25M_\odot$ for all initial rotational velocities. As expected, the Vink wind results in significantly higher mass loss rates as compared to the Björklund wind, with the difference shrinking as the masses get larger. Here, the bumps corresponding with the transition to the low-temperature Vink wind are also clearly visible.

The plots also show an elevated mass loss rate for Milky Way metallicity, aligning with theoretical expectations. Metals, abundant in spectral lines, are more effective at absorbing and re-emitting radiation, thereby experiencing increased radiation pressure. Consequently, the higher metallicity in the Milky Way facilitates stronger radiation-driven winds.

4.3. Rotational evolution

In Fig 3 and 4, the rotational evolution of 5, 15, and $25M_\odot$ stars are plotted for all initial rotational velocities, for LMC and Milky Way metallicity respectively.

In comparison to Fig. 2 from Hastings et al. (2020), our findings for Milky Way metallicity with $v_{\rm init} = 0.6$ display a lower maximum $v_{\rm rot}/v_{\rm crit}$ under the Vink wind prescription. While the implementation of the Vink wind in MESA aims to replicate the results observed in Brott et al. (2011), there are a lot of variables at play. Determining the precise cause of the observed discrepancies exceeds the scope of this project but presents an opportunity for future research.

The Björklund wind, characterised by lower mass loss rates and consequently less angular momentum loss compared to the Vink

prescription, consistently results in higher $v_{\rm rot}/v_{\rm crit}$ values. This allows a significant number of stars within our simulation grid to achieve critical velocities, with stars having higher initial velocities reaching this critical threshold earlier in their evolution. In contrast, the Vink wind shows a strong decrease in rotational velocity at the later stages of main-sequence evolution, primarily due to the enhanced mass loss rates triggered at the effective temperature jump $T_{\rm eff}^{\rm jump}$. This bi-stability jump leads to a strong decrease in stellar rotation.

The impact of metallicity is most pronounced in the Vink wind models, where stars with LMC metallicity can spin up more. This effect is largely attributed to the HR diagram positioning of LMC metallicity tracks, which tend to be hotter and therefore reach the bi-stability jump later in their evolutionary sequence.

It has to be noted that MESA does not allow a $v_{\rm rot}/v_{\rm crit}$ larger than 1. At this point, the surface material is shedded and we can assume it collects in a circumstellar disk, forming a Be star.

4.4. Final rotation

In Fig. 5, the final rotational velocity $v_{\rm rot}/v_{\rm crit}$ in terms of the initial velocity is plotted for the entire grid of simulations. To exclude the final stages of the main-sequence evolution, corresponding to the 'hook' on the HR diagram, the final $v_{\rm rot}/v_{\rm crit}$ is determined at the minimum temperature in their evolution. The only two exceptions are the two tracks we mentioned at the end of 4.1. For these two cases the final $v_{\rm rot}/v_{\rm crit}$ was determined when the central hydrogen fraction reached 0.011.

We will refer to this value as the final rotation $v_{\rm final}$:

$$v_{\rm final} = \frac{\text{Final } v_{\rm rot}/v_{\rm crit}}{\text{Initial } v_{\rm rot}/v_{\rm crit}}$$

For the Vink wind, the overall trend indicates that $v_{\rm final}$ drops off with higher masses and with higher initial velocities, which is expected as both increase mass loss due to stellar winds. For the Björklund wind, a large part of the grid reaches the critical velocity. The big difference between the Vink and Björklund wind can be attributed to the bi-stability jump, which significantly slows down the stars with the Vink wind as they cross $T_{\rm eff}^{\rm jump}$.

4.5. Reaching threshold velocity

In the context of Be star formation, it is more insightful to check whether stars reach a specific threshold velocity at any point during their main sequence phase, rather than only assessing the velocity at the final stages of their main sequence evolution. Fig. 6 presents an analysis of the conditions under which stars achieve certain threshold velocities prior to the hook in their HR tracks. As discussed in the introduction, the precise rotational speed required for Be star formation remains uncertain, therefore we have selected threshold values in the upper range of $v_{\rm rot}/v_{\rm crit}$: 0.6, 0.7, and 0.8.

A clear pattern emerges from the data: the Björklund wind prescription consistently enables a broader segment of the simulation grid to reach these threshold velocities. In no instance does the Vink wind reach a threshold velocity where the Björklund wind does not. It is important to note that the Björklund wind was applied across all initial masses, including those lower than recommended for this model. However, this trend remains valid for stars with initial masses of $15M_\odot$ and above.

Examining the instances where the Vink wind reaches the threshold velocity reveals a distinct pattern. As mass increases from 5 to $\sim 10M_\odot$, the stars encounter greater difficulty in spinning up due to enhanced mass loss from stronger winds. Beyond this, from around $10M_\odot$ to $15M_\odot$, the efficiency of internal angular momentum transport improves and compensates for the braking effect of stellar winds, allowing stars with lower initial velocities to achieve the threshold velocities. As the mass continues to increase, the influence of stellar winds intensifies, necessitating higher initial velocities to reach the threshold.

This pattern is not observed with the Björklund wind, where the impact of stellar winds is consistently smaller across all masses. Consequently, the enhancement in internal angular momentum transport with increasing initial mass results in higher masses achieving the threshold velocities more easily.

5. Conclusion

We utilised the MESA code to simulate the main-sequence evolution of a grid of stars under two different wind prescriptions, Vink and Björklund, across varying metallicities, initial masses, and rotational velocities. The objective was to explore potential single-star evolutionary channels for the formation of Be stars, focusing on the effects of mass loss and rotational evolution influenced by the selected wind models.

The results indicate that the Björklund wind prescription, characterised by its lower mass loss rates, allows stars to retain more of their angular momentum compared to the Vink prescription. This difference significantly affects the rotational evolution of the stars, with those under the Björklund prescription often reaching higher rotational velocities, and thus more closely approaching or reaching the critical rotational speeds that could be necessary for Be star formation. Notably, the Björklund model enabled a significant portion of our simulation grid, across a broad range of initial conditions, to achieve or exceed certain rotational velocity thresholds at some point during their main-sequence lifetimes.

Conversely, with its stronger winds, particularly after crossing the bi-stability jump, the Vink wind exhibits a strong mass loss that substantially reduces rotational speed. Often these wind-induced losses were sufficient to prevent these stars from reaching higher rotational velocities.

Additionally, the study highlighted the importance of metallicity in the evolution of stellar rotation. Stars with Milky Way metallicity experience higher mass loss rates due to the greater efficiency of radiation-driven wind mechanisms in metal-rich environments, affecting their rotational velocities.

In summary, our findings underscore the significant role of wind prescriptions in stellar evolution, particularly in the formation mechanisms of Be stars. The Björklund wind allows for higher rotational velocities, offering a possible pathway to Be star formation through single-star evolution.

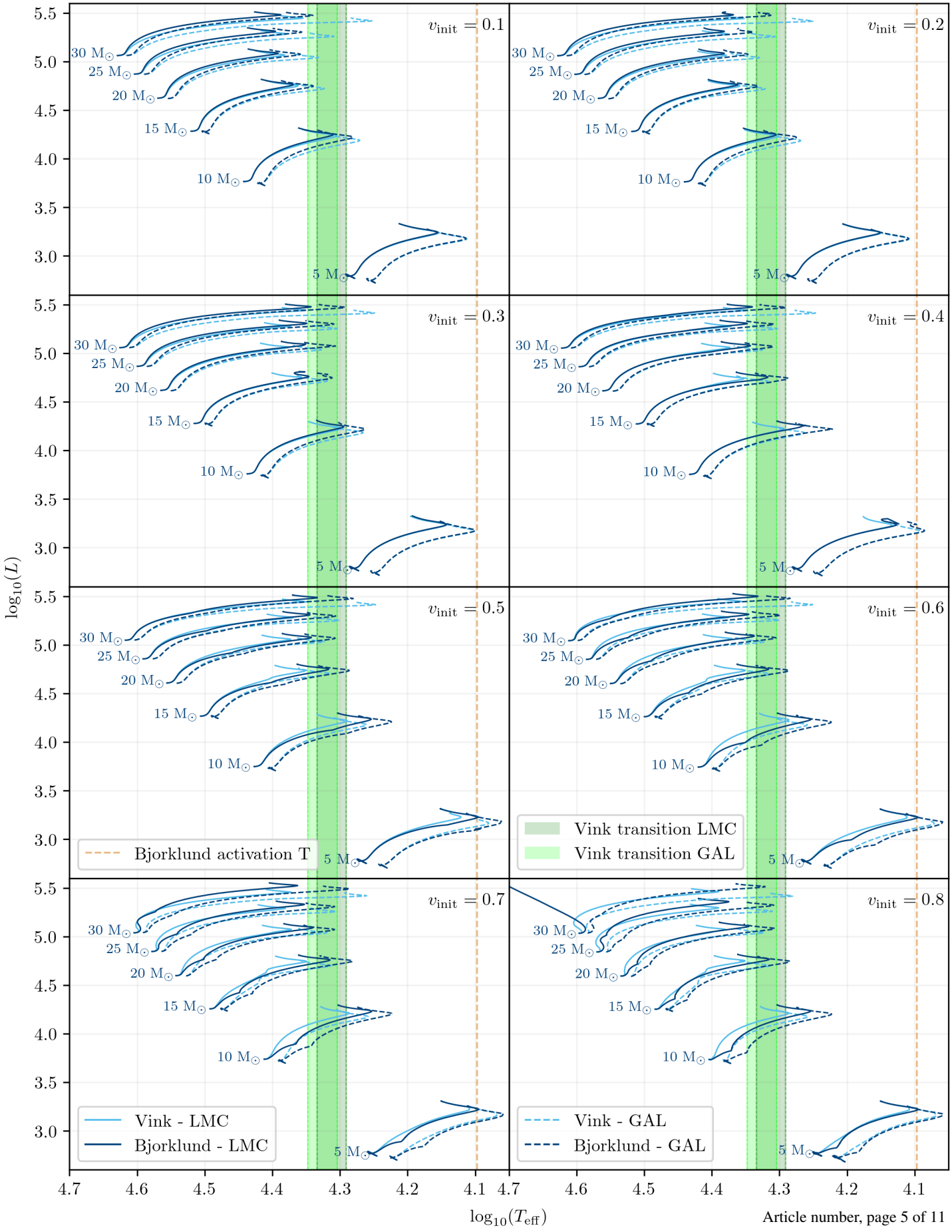

Fig. 1: HR tracks for Vink and Björklund wind, full lines for LMC metallicity and dashed lines for Mily Way metallicity.

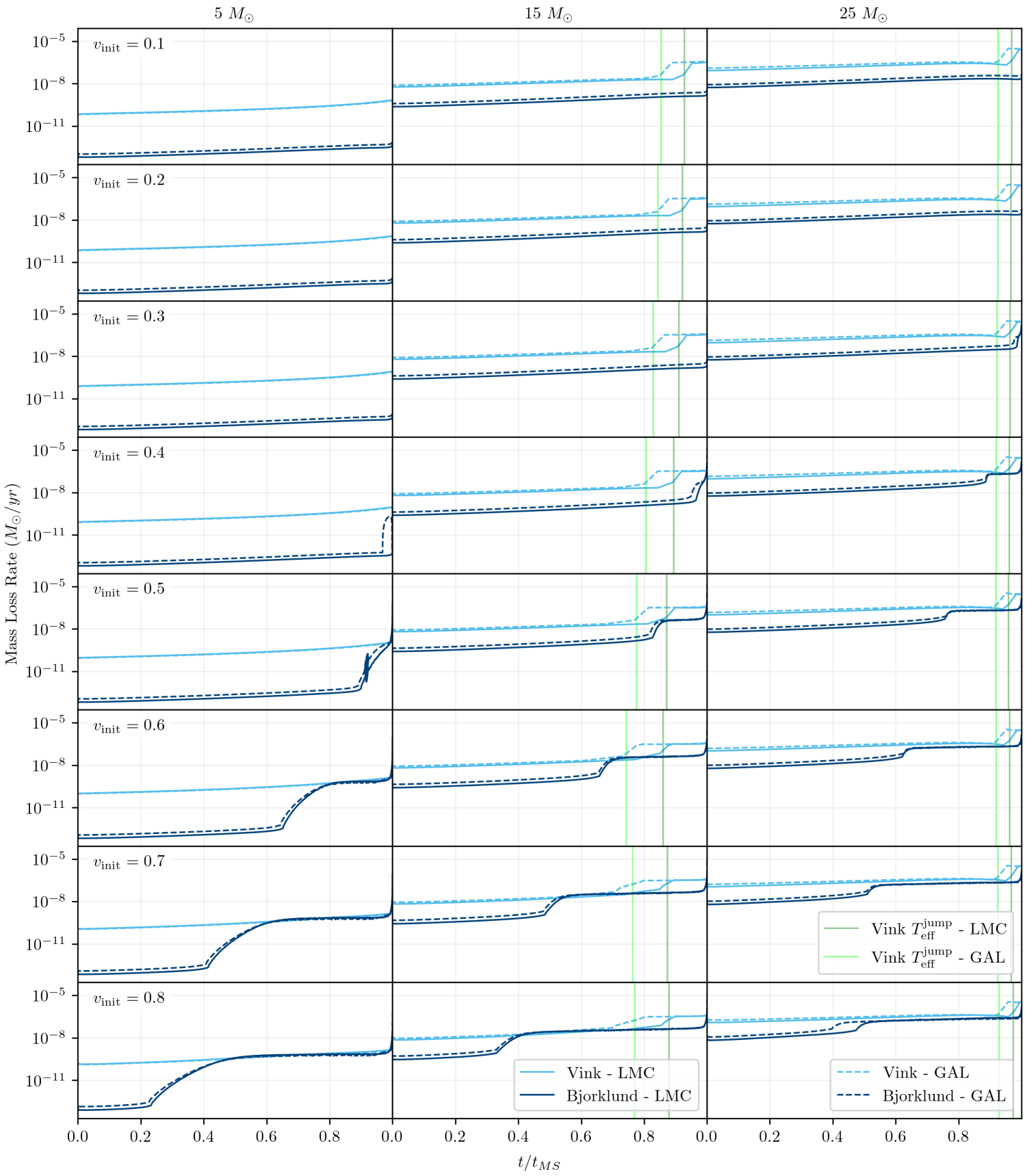

Fig. 2: mass loss rates for Vink and Björklund wind, full lines for LMC metallicity and dashed lines for Mily Way metallicity.

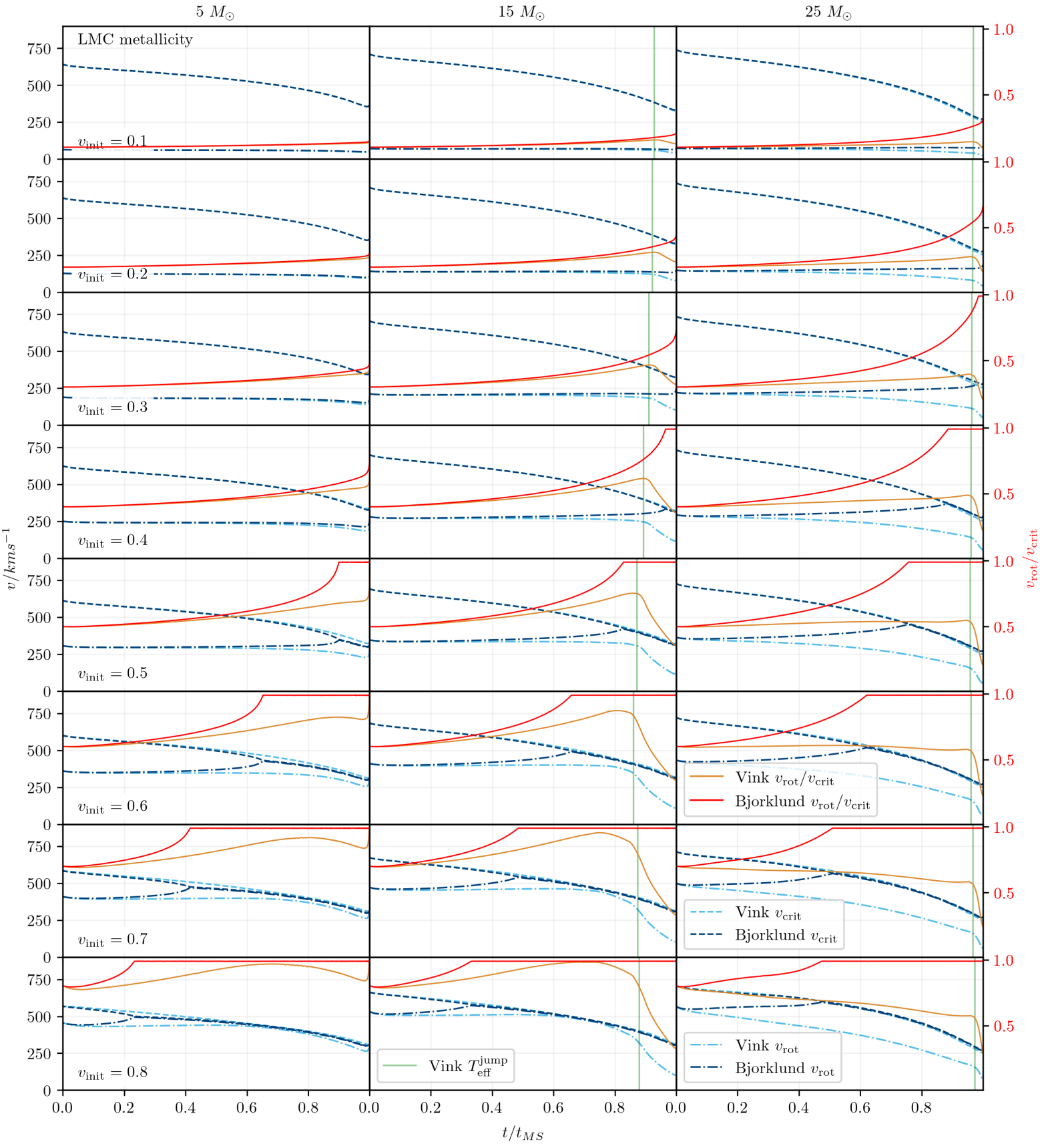

Fig. 3: Evolution of the equatorial rotation of Vink and Björklund wind at LMC metallicity.

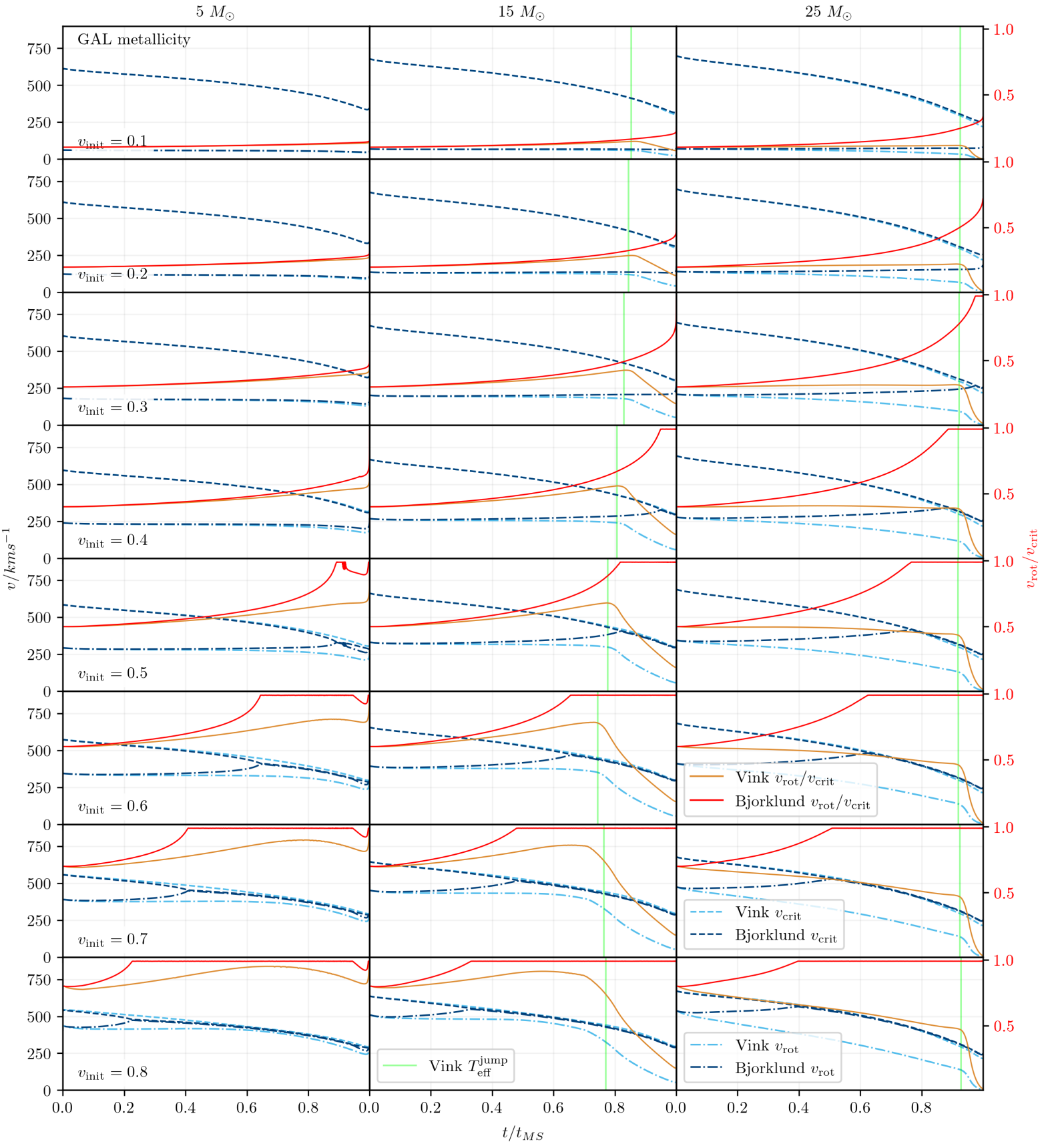

Fig. 4: Evolution of the equatorial rotation of Vink and Björklund wind at Milky Way metallicity.

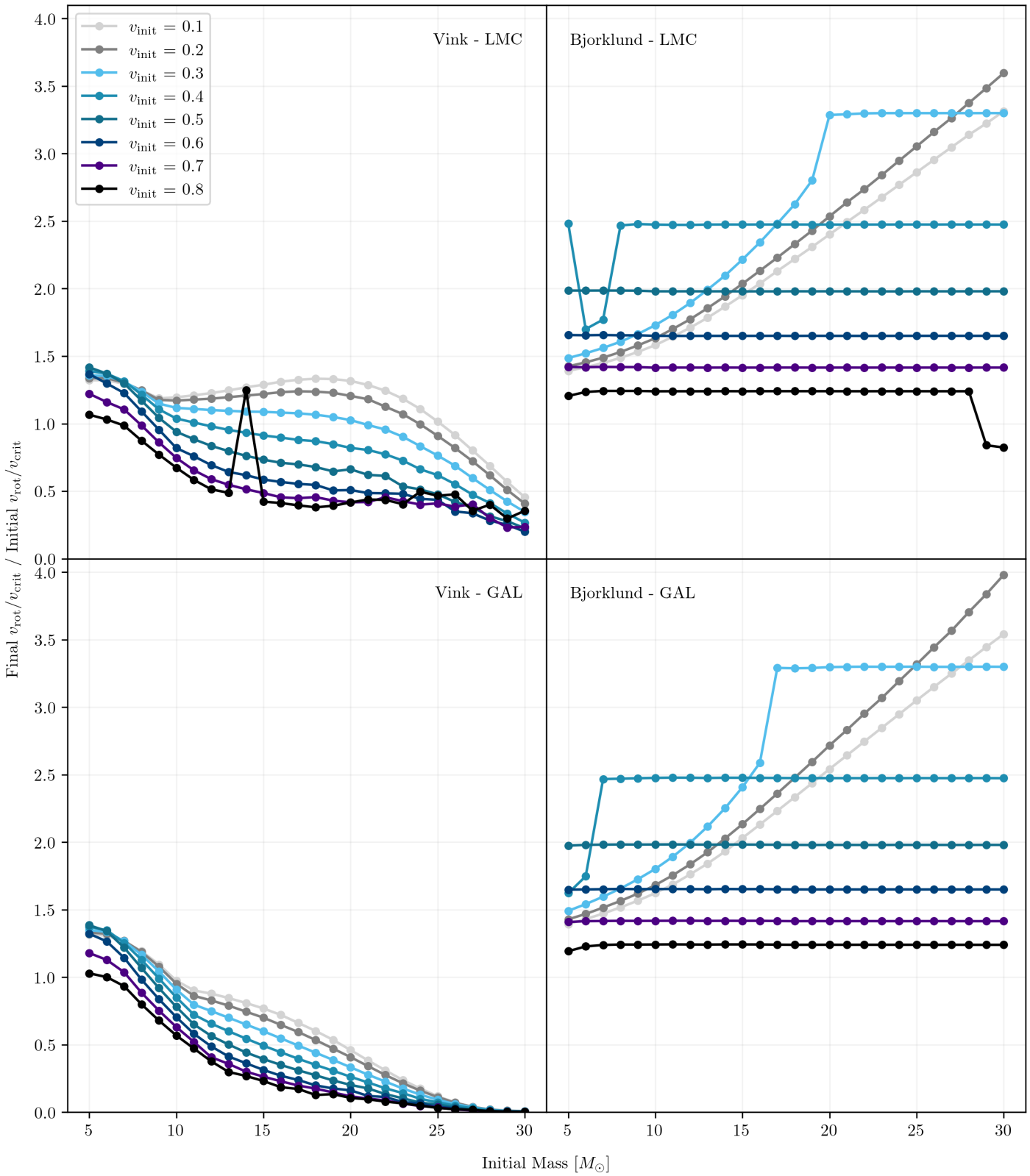

Fig. 5: Final rotational velocities compared to the initial rotational velocities for the entire grid of simulations.

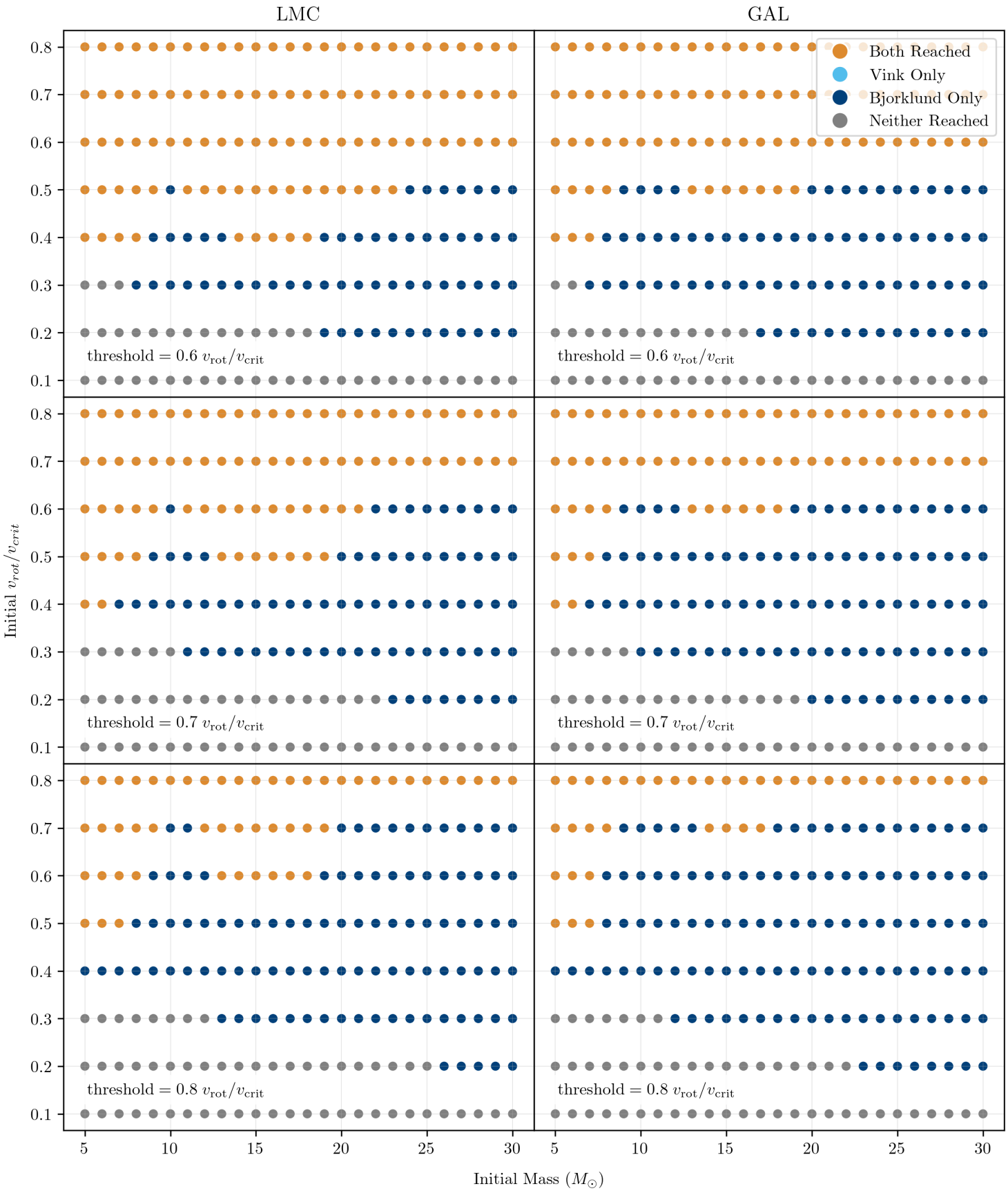

Fig. 6: Plot showing which simulation conditions allow a star to reach a certain threshold velocity.

References

Baschek, B., Kegel, W. H., & Traving, G. 1975, Problems in stellar atmospheres and envelopes
Björklund, R., Sundqvist, J. O., Singh, S. M., Puls, J., & Najarro, F. 2022, New predictions for radiation-driven, steady-state mass-loss and wind-momentum from hot, massive stars III. Updated mass-loss rates for stellar evolution
Brott, I., de Mink, S. E., Cantiello, M., et al. 2011, A&A, 530, A115
Hamann, W. R., Koesterke, L., & Wessolowski, U. 1995, A&A, 299, 151
Hastings, B., Wang, C., & Langer, N. 2020, A&A, 633, A165
Huang, W., Gies, D. R., & McSwain, M. V. 2010, ApJ, 722, 605
Nieuwenhuijzen, H. & de Jager, C. 1990, A&A, 231, 134
Paxton, B. 2019, Modules for Experiments in Stellar Astrophysics (MESA)
Paxton, B., Bildsten, L., Dotter, A., et al. 2010, MESA: Modules for Experiments in Stellar Astrophysics, Astrophysics Source Code Library, record ascl:1010.083
Paxton, B., Cantiello, M., Arras, P., et al. 2013, ApJS, 208, 4
Paxton, B., Marchant, P., Schwab, J., et al. 2015, ApJS, 220, 15
Paxton, B., Schwab, J., Bauer, E. B., et al. 2018, ApJS, 234, 34
Raguzova, N. V. & Popov, S. B. 2005, Astronomical and Astrophysical Transactions, 24, 151
Rivinius, T., Carciofi, A. C., & Martayan, C. 2013, A&A Rev., 21, 69
Spruit, H. C. 2002, A&A, 381, 923
Struve, O. 1931, ApJ, 73, 94
Townsend, R. H. D., Owocki, S. P., & Howarth, I. D. 2004, Monthly Notices of the Royal Astronomical Society, 350, 189
Vink, J. S., de Koter, A., & Lamers, H. J. G. L. M. 2001, A&A, 369, 574
Zorec, J., Frémat, Y., Domiciano de Souza, A., et al. 2016, A&A, 595, A132